

This is the Accepted Manuscript version of an article accepted for publication in Journal colloid and interface science. Elsevier is not responsible for any errors or omissions in this version of the manuscript or any version derived from it.

The Version of Record is available online at

<https://doi.org/10.1016/j.jcis.2021.09.192>

Luigi Gentile,

Ferrihydrite nanoparticles entrapped in shear-induced multilamellar vesicles,

Journal of Colloid and Interface Science,

Volume 606, Part 2,

2022,

Pages 1890-1896,

ISSN 0021-9797,

<https://doi.org/10.1016/j.jcis.2021.09.192>.

(<https://www.sciencedirect.com/science/article/pii/S0021979721016568>)

1  
2  
3  
4  
5  
6  
7  
8 **Ferrihydrite nanoparticles entrapped in shear-**  
9  
10  
11  
12 **induced multilamellar vesicles**  
13  
14  
15  
16  
17

18 *Luigi Gentile*<sup>1,2\*</sup>  
19  
20

21 1. Department of Chemistry, University of Bari “Aldo Moro”, Via Orabona 4, Bari, 70126, Italy  
22

23  
24 2. Center of Colloid and Surface Science (CSGI) Bari Unit, Via Orabona 4, Bari, 70126, Italy  
25  
26  
27

28 **AUTHOR INFORMATION**  
29  
30

31 **Corresponding Author**  
32  
33

34 \*Luigi Gentile, Senior Lecturer, Department of Chemistry, University of Bari “Aldo Moro”,  
35  
36 70125 Bari (Italy) [orcid.org/0000-0001-6854-2963](https://orcid.org/0000-0001-6854-2963) email: [luigi.gentile@uniba.it](mailto:luigi.gentile@uniba.it), Tel: +39  
37  
38 0805442033.  
39  
40  
41  
42

43 **Abstract**  
44  
45  
46

47 *Hypothesis*  
48  
49

50 Ferrihydrite (Fh) nanoparticles are receiving considerable scientific interest due to their large  
51 reactive surface areas, crystalline structures, and nanoparticle morphology. They are of great  
52 importance in biogeochemical processes and have the ability to sequester hazardous and toxic  
53 substances. Here, the working hypothesis was to entrap fractal-like Fh nanoparticles, with a radius  
54 of gyration of 6.2 nm and a primary building block of polydisperse spheres with a radius of 0.8  
55  
56  
57  
58  
59  
60  
61  
62  
63  
64  
65

1  
2  
3  
4 nm, in a shear-induced multilamellar vesicle (MLV) state using a 40 wt.% polyethylene glycol  
5  
6 dodecyl ether surfactant.  
7  
8

### 9 *Experiments*

10  
11 Small- and Wide- Angle X-ray scattering revealed the equilibrium state of the non-ionic planar  
12  
13 lamellar phase, the Fh dispersion, and their mixture. The MLV state was induced by using a shear  
14  
15 flow in a Taylor-*Couette* geometry of a rheometer.  
16  
17

### 18 *Findings*

19  
20  
21 The nonionic surfactant initially exhibited a lamellar gel phase with two distinct *d*-spacings of 11.0  
22  
23 and 9.7 nm, which collapsed into the MLV state under shear flow. The Fh nanoparticles induced  
24  
25 bilayer attraction by suppressing lamellar layer undulations, decreasing the *d*-spacing. These  
26  
27 results are helpful in the understanding of the relationship between nanoparticle size and  
28  
29 nanoparticle-bilayers interactions and provides insight on Fh encapsulations in a kinetically stable  
30  
31 MLVs state.  
32  
33  
34  
35  
36

37 **Keywords.** Ferrihydrite, lamellar phase, vesicles, shear-induced transition, rheology, SAXS.  
38  
39  
40  
41  
42  
43  
44

## 45 **1. Introduction**

46  
47 Ferrihydrite, Fh, is a hydrous ferric oxide mineral with a low degree of crystallinity copious in  
48  
49 natural environments. Due to its large reactive surface area, it is involved in several  
50  
51 biogeochemical processes.[1,2] Moreover, Fh is able to sequester and remove anionic dyes, which  
52  
53 are toxic to living organisms.[3] Its crystalline structure has been debated due to its fine particle  
54  
55 size and indeterminate structure and composition.[2,4] Recently, it has been found to consist of  
56  
57 sheets of edge-sharing Fe-O octahedra, interspersed with sheets consisting of coexisting Fe-O  
58  
59  
60  
61  
62  
63  
64  
65

1  
2  
3  
4 octahedra and Fe-O tetrahedra, arranged in a hexagonal unit cell (space group P63mc).[5,6] X-ray  
5  
6 diffraction has distinguished “two-line ferrihydrite” (two peaks in the patterns) as the least ordered  
7  
8 form up to “six-line ferrihydrite” in its more ordered form. Here we focus on six-line ferrihydrite.  
9

10  
11  
12 In nature and after synthesis, ferrihydrite occurs as nanoparticles ranging from 1 to 10 nm fully  
13  
14 dispersed or aggregated in a fractal cluster.[6–8] The presence of surface groups in six-line Fh  
15  
16 particles makes their shell water-rich, while their mineral core results hydrogen-poor.[6] pH and  
17  
18 aging over time have a strong effect on Fh aggregates. A pH of 3.5 increases electrostatic repulsion,  
19  
20 disaggregating clusters into their primary nanoparticles. On the other hand, aging leads to CO<sub>2</sub>  
21  
22 adsorption, resulting in surface-adsorbed carbonate species[9] that prevent formation of metastable  
23  
24 surface clusters toward the point of zero charge at around pH 8.[10] Nanoparticles are able to  
25  
26 adsorb organic material at this interface[11] and their dynamics in polymer networks is the subject  
27  
28 of intensive study.[12] Hiemstra[2] provided thermodynamic data for determining the solubility  
29  
30 product for freshly prepared six-line Fh over a size range of 2.5-4 nm,  $\log([Fe^{3+}][OH^-]^3) =$   
31  
32  $\log K_{so} \sim 39.5$ . The smallest particles in an Fh suspension react according to the Ostwald–  
33  
34 Freundlich equation  $RT\Delta \ln K_{so} = 2/3 \gamma A$ , where A is the surface area and  $\gamma$  ( $\approx 0.19 \text{ J m}^{-2}$ ) is the  
35  
36 interfacial tension [2], while the Fh suspension as whole reacts in line with the Ostwald equation  
37  
38  $RT\Delta \ln K_{so} = \gamma A$ . The colloidal stability of Fh suspension is affected by several parameters such  
39  
40 as initial size, pH, aging, and concentration that could lead to aggregation and eventually  
41  
42 precipitation.  
43  
44  
45  
46  
47  
48  
49  
50  
51

52  
53 Here, an Fh nanoparticle dispersion was entrapped in a non-ionic lamellar phase to increase  
54  
55 stability and to evaluate the effect on the lamellar phase. An aged six-line Fh dispersion (pH ~6.5)  
56  
57 was used to prepare a 40 wt.% lamellar phase using tetraethylene glycol monododecyl ether  
58  
59 (C<sub>12</sub>E<sub>4</sub>) with Mn ~362, known as Brij® L4 (L4). C<sub>n</sub>E<sub>m</sub> surfactants are well known to form planar  
60  
61  
62  
63  
64  
65

1  
2  
3  
4 lamellar phase ( $L\alpha$ ) morphology[13] even in mixed systems,[14] which under shear flow collapse  
5  
6 into multilamellar vesicle (MLV) morphology; this is known as the  $L\alpha$ -to-MLV transition.[15–19]  
7  
8 The  $d$ -spacing, i.e. layer spacing of the lamellae, for pure  $C_{12}E_4$  at 40 wt.% in  $D_2O$  is 6.8 nm.[20–  
9  
10 22] However, Brij® L4 is not a pure  $C_{12}E_4$  and may contain fractions of other  $C_nE_m$ .  
11  
12  
13

## 14 15 **2. Materials and methods**

### 16 17 **2.1 Materials**

18  
19  
20 Materials. Brij® L4 nonionic surfactant made of polyethylene glycol dodecyl ether with Mn  
21  
22 ~362 (i.e. ~ tetraethylene glycol monododecyl ether,  $C_{12}E_4$ ), was purchased from Levanchimica  
23  
24 Srl (Bari, Italy). The L4 lamellar phase was prepared by mixing 40 wt.% of the surfactant with  
25  
26 distilled  $H_2O$  (labeled L4-40wt). Six-line ferrihydrite (Fh) was synthesized as reported by  
27  
28 Schwertmann and Cornell [1] by dissolving 18 g of  $Fe(NO_3)_3 \cdot 9H_2O$  in 2 L of preheated distilled  
29  
30 water by applying a continuous stirring. The suspension was kept at 75 °C for 11 min and then  
31  
32 rapidly cooled to room temperature. The suspension was dialyzed against Milli-Q water to remove  
33  
34 nitrates with a membrane cutoff of 12–14 kDa (Spectrum Laboratories Inc., Rancho Dominguez,  
35  
36 USA) until the electrical conductivity was less than  $5 \mu S m^{-1}$ . The solid concentration of Fh in the  
37  
38 final nanoparticle dispersion was measure by solvent-evaporation and it was 1.6 g/l. The dispersion  
39  
40 is affected by aging [7] and as such has been used after two years showing a final pH of ~6.5. The  
41  
42 obtained dispersion was then diluted with  $H_2O$  to obtain a 60 wt. % dispersion comparable with  
43  
44 the nanoparticles concentration in the L4/ferrihydrite system (labeled L4Fh-40wt). L4-40wt and  
45  
46 L4Fh-40wt systems were heated (~80°C) and stirred, cooling down to room temperature, to obtain  
47  
48 a metastable lamellar phase.  
49  
50  
51  
52  
53  
54  
55  
56

### 57 58 **2.2 Small- and Wide-Angle X-ray Scattering (SAXS and WAXS)**

59  
60  
61  
62  
63  
64  
65

1  
2  
3  
4 SAXS and WAXS measurements were performed using a pinhole-collimated system equipped  
5  
6 with a Genix 3D X-ray source (Xenocs SA, Sassenage, France), namely SAXSLab Ganesha  
7  
8 300XL instrument (SAXSLAB ApS, Skovlunde, Denmark). The scattering intensity,  $I(q)$ , was  
9  
10 recorded with the Pilatus detector (Dectris Ltd, Baden, Switzerland) located at three distinct  
11  
12 distances from the sample, yielding a scattering vector range  $0.0042 \text{ \AA}^{-1} \leq q \leq 1.75 \text{ \AA}^{-1}$ . Samples  
13  
14 were loaded in a 1.5 mm diameter quartz capillary and then sealed (Hilgenberg GmbH, Malsfeld,  
15  
16 Germany). An external JULABO thermostat (JULABO, Seelbach, Germany) fixed to 25 °C  
17  
18 controlled the temperature. The two-dimensional (2D) scattering pattern was radially averaged  
19  
20 using SAXSGui v2.15.01 software to obtain  $I(q)$ . The measured scattering curves were corrected  
21  
22 for the background scattering.  
23  
24  
25  
26  
27  
28

## 29 30 **2.3 Rheology**

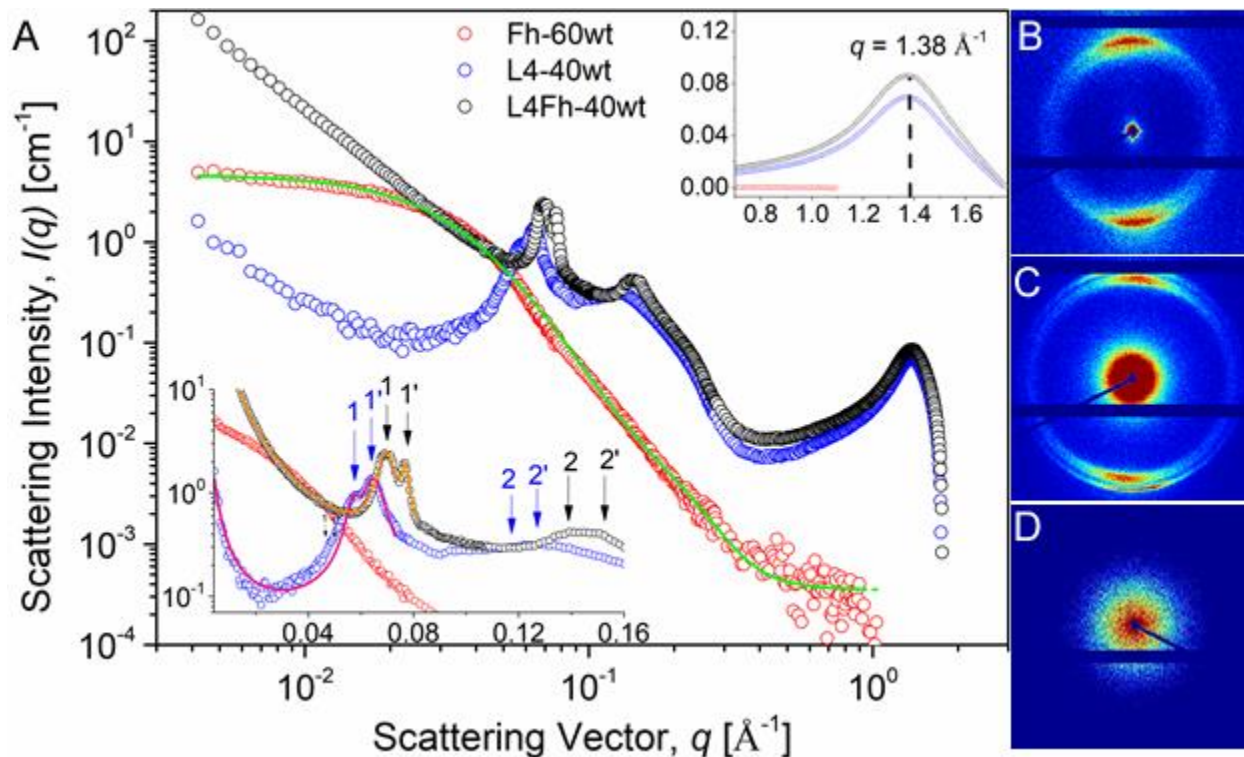
31  
32 Step rate tests of 900 s were employed as transient experiments to induce a lamellar-to-MLV  
33  
34 transition in the L4-40wt and L4Fh-40wt systems, respectively. Upward stepped ramps of shear  
35  
36 rates in the range from 0.1 to 100 s<sup>-1</sup> identified the onset of the transition for both systems.  
37  
38 Rheological measurements were carried out using the MCR302e stress-controlled rheometer  
39  
40 (Anton Paar GmbH, Graz, Austria) equipped with a Taylor-Couette geometry, *i.e.* concentric  
41  
42 cylinder geometry, (inner diameter of 16.662 mm and a gap of 0.704 mm). The temperature was  
43  
44 kept to 25 °C by a Peltier system.  
45  
46  
47  
48  
49

## 50 51 **3. Results and discussion**

### 52 53 **3.1 Structural features at the equilibrium**

54  
55  
56 Figure 1 shows the joint small- and wide-angle X-ray scattering (SAXS and WAXS) profiles for  
57  
58 a 40 wt.% L4 non-ionic lamellar phase (L4-40wt), the Fh dispersion diluted with 40 wt.% H<sub>2</sub>O to  
59  
60  
61  
62  
63  
64  
65

1  
2  
3  
4 achieve the same concentration as the mixed sample (Fh-60wt), and the 40 wt.% L4 non-ionic  
5  
6 lamellar phase prepared in the Fh dispersion (L4Fh-40wt).  
7  
8  
9



10  
11  
12  
13  
14  
15  
16  
17  
18  
19  
20  
21  
22  
23  
24  
25  
26  
27  
28  
29  
30  
31  
32  
33  
34  
35  
36  
37 **Figure 1.** Radially averaged small- and wide-angle X-ray scattering (SAXS and WAXS) profiles  
38  
39 (A) at 25 °C of 60 wt.% in water of the ferrihydrite nanoparticle dispersion (Fh-60wt; red dot), i.e.  
40  
41 0.96 g/l, 40 wt.% L4 nonionic surfactant in H<sub>2</sub>O (L4-40wt; blue dot), and 40 wt. % L4 nonionic  
42  
43 surfactant in Fh nanoparticle dispersion (L4Fh-40wt; black dot). The green line shows the best fit  
44  
45 for a fractal structure with a primary building block of polydisperse spheres, based on the Teixeira  
46  
47 model,[23] eq. 1-3. The bottom-left inset shows a semi-log plot of the scattering profiles along  
48  
49 with the best fit for the lamellar phase following Prevost *et al.*,[24] eq. 4, for the L4-40wt (pink)  
50  
51 and L4Fh-40wt (orange) samples. The top-right inset shows a linear-linear plot of the WAXS  
52  
53 profiles, with a peak at  $q = 1.38 \text{ \AA}^{-1}$  for both the L4-40wt and L4Fh-40wt samples. 2D SAXS  
54  
55 pattern in the low  $q$ -range for L4-40wt (B), L4Fh-40wt (C) and Fh-60wt (D).  
56  
57  
58  
59  
60  
61  
62  
63  
64  
65

The Fh dispersion scattering profiles are consistent with fractal-like aggregates with a primary building block of polydisperse spheres following the Teixeira model,[23] where the sphere radius is described by the Schulz distribution,

$$I(q)_{Fh} = P(q)_{pS}S(q)_{Teix} + bg \quad (1)$$

where  $P(q)_{pS}$  is the form factor of the polydisperse sphere,

$$P(q)_{pS} = \phi V_p \Delta\rho^2 \int f_{Sch}(R_0, \bar{R}_0, \sigma) \left[ \frac{3[\sin(qR_0)] - qR_0 \cos(qR_0)}{(qR_0)^3} \right]^2 dR_0 \quad (2)$$

and where  $\phi$  is the volume fraction of the particles,  $V_p$  is the volume of a single particle,  $\Delta\rho$  is the scattering length density differences,  $R_0$  is the particle radius, and  $\sigma$  is the standard deviation of the Schulz distribution  $f_{Sch}$ , fixed here as 0.35. Based on the curve-fitting,  $R_0 = 0.8$  nm, in agreement with Guénet *et al.*[25] and with the dynamic light scattering data in the supplementary material.

$S(q)_{Teix}$  is the Teixeira structure factor,[23]

$$S(q)_{Teix} = 1 + \frac{\sin[(D-1)\tan^{-1}(q\xi)]}{(qR_0)^D} \frac{D\Gamma(D-1)}{[1 + 1/(q^2\xi^2)]^{(D-1)/2}} \quad (3)$$

where  $\Gamma$  is the gamma function,  $D$  (equal to 3.2) is the fractal dimension, indicating a surface fractal, and  $\xi$  is the correlation length of 2.4 nm. Thus,  $R_g = \sqrt{D(D+1)\xi^2/2} = 6.2$  nm, which is in line with the fractal aggregate size reported by Guénet *et al.*[25] of around 6 nm. However, these results differ from those of a previous study,[7] in which repulsive inter-particle interactions result in a structure factor which is different from 1 and a particle radius of 2.7 nm,[7] while yet other studies have reported a particle radius of 1.3 nm.[26–28] These differences may be due to higher adsorption of CO<sub>2</sub> on the nanoparticle surface when aged over a longer period (2 years) that results in a pH increase.

1  
 2  
 3  
 4 The L4 lamellar phase exhibited a peak in the WAXS region centered at  $q_{WAXS} = 1.38 \text{ \AA}^{-1}$ , i.e.  
 5  
 6  $d_{WAXS} = 0.455 \text{ nm}$ , which implies lateral packing of alkyl chains perpendicular to the bilayer,  
 7  
 8 indicating a gel lamellar phase  $L_{\beta}$ . [29–32] The  $q_{WAXS}$  peak arises from the samples as shown in the  
 9  
 10 supplementary material. Several models for fitting scattering data for lamellar phases have been  
 11  
 12 suggested in the literature. [24,33–35] Here we adopted a model based on the Prevost *et al.* [24]  
 13  
 14 approach, in which the scattered intensity arises from the lamellae stacking, described by a  
 15  
 16 Lorentzian peak, with an initial increase due to diffuse small-angle scattering coming from local  
 17  
 18 fluctuations in the surfactant concentration (layer undulation). However, two lamellar peaks can  
 19  
 20 be observed in the 1D scattering profile (Figure 1) as well as in the 2D scattering profile, where  
 21  
 22 two distinct pairs of Bragg peaks were detected, implying two lamellar phases. Moreover, two  
 23  
 24 additional peaks were detected with a relative position ratio of 1:2 (bottom-left inset of Figure 1),  
 25  
 26 due to the (100) and (110) reflections of the lamellar phase. [36,37] The presence of two lamellar  
 27  
 28 spacing might be ascribed to the metastable state obtain during preparation. Further studies will be  
 29  
 30 conducted on the equilibrium phase. The inter-lamellar distance ( $d$ -spacing) can be calculated from  
 31  
 32 the  $q$  value of the first peak as  $d_{L\beta 1} = 2\pi/q_{L\beta 1}^{peak}$  and  $d_{L\beta 2} = 2\pi/q_{L\beta 2}^{peak}$ , where  $q^{peaks}$  is the center  
 33  
 34 of the respective Bragg peaks. We have assumed that both lamellar phases,  $L_{\beta 1}$  and  $L_{\beta 2}$ , are in the  
 35  
 36 gel phase, although it is difficult to discriminate between them. Thus, the Prevost *et al.* [24]  
 37  
 38 equation taking into account the two coexisting lamellar phases takes the following form,  
 39  
 40  
 41  
 42  
 43  
 44  
 45  
 46  
 47  
 48  
 49  
 50  
 51  
 52  
 53  
 54  
 55  
 56  
 57  
 58  
 59  
 60  
 61  
 62  
 63  
 64  
 65

$$\begin{aligned}
 I(q)_{L\alpha} = & \frac{I_{L\beta 1}(0)}{1 + (q\zeta_{L\beta 1})^2} + \frac{I_{L\beta 2}(0)}{1 + (q\zeta_{L\beta 2})^2} + \frac{I_{L\beta 1}}{1 + \left[ (q - q_{L\beta 1}^{peak}) \zeta_{L\beta 1}^{peak} \right]^2} \\
 & + \frac{I_{L\beta 2}}{1 + \left[ (q - q_{L\beta 2}^{peak}) \zeta_{L\beta 2}^{peak} \right]^2} \quad (4)
 \end{aligned}$$

1  
2  
3  
4  
5  
6 where  $I_{L\beta_1}(0)$ , and  $I_{L\beta_2}(0)$  are intensity scaling factors and  $I_{L\beta_1}$  and  $I_{L\beta_2}$  are the Bragg peak  
7  
8 intensities.  $\zeta_{L\beta_1}$  and  $\zeta_{L\beta_2}$  are the correlation lengths of the surfactant concentration fluctuations,  
9  
10 while  $\zeta_{L\beta_1}^{peak}$  and  $\zeta_{L\beta_2}^{peak}$  are the inter-membrane correlation lengths (perpendicular to the membrane  
11  
12 plane). As reported by Castro-Roman *et al.*[38] the layer undulations are taken into account in a  
13  
14 non-self-consistent way in the Nallet model,[39] which is similar to the Prevost *et al.*[24] model.  
15  
16 Here, the purpose is to determine the mean distance between the lamellar sheets. The L4 lamellar  
17  
18 phase prepared in the Fh dispersion (L4Fh-40wt) exhibited Bragg peaks similar to the original L4  
19  
20 lamellar phase, while better defined at a higher  $q$ -position. The (110) reflections are also more  
21  
22 pronounced than in the nanoparticles-free lamellar phase. At low- $q$  a power law of 2.2 was  
23  
24 observed, might due to smaller bilayer undulations than in the L4 prepared in water. However, the  
25  
26 power law in the L4Fh-40wt sample may have been affected to some extent by fractal aggregation  
27  
28 of the Fh nanoparticles. It is worth noting that no phase separation was observed several months  
29  
30 after preparation. The two  $d$ -spacings obtained from eq. 4 for the L4 lamellar phase in water (L4-  
31  
32 40wt) and L4 in Fh dispersion (L4Fh-40wt) are reported in Table 1.  
33  
34  
35  
36  
37  
38  
39  
40  
41  
42  
43

44 **Table 1.**  $d$ -spacing  $d_{L\beta_1} = 2\pi/q_{L\beta_1}^{peak}$  and  $d_{L\beta_2} = 2\pi/q_{L\beta_2}^{peak}$  for the 40 wt.% L4 lamellar phase in  
45  
46 water (L4-40wt) and in the ferrihydrite dispersion (L4Fh-40wt), where  $q_{L\beta_1}^{peak}$  and  $q_{L\beta_2}^{peak}$  were  
47  
48 obtained from SAXS profile fitting (eq. 4), and where  
49  
50  $I_{L\beta_1}$  and  $I_{L\beta_2}$  are the relative intensities. The theoretical maximum inter-lamellar  $d$ -spacing was  
51  
52 calculated using eq. 5. All values are in nm.  
53  
54  
55  
56

| $d_{L\beta_1}$ | $d_{L\beta_2}$ | $I_{L\beta_1}$ | $I_{L\beta_2}$ | $d_{L\beta}^{max}$ |
|----------------|----------------|----------------|----------------|--------------------|
|----------------|----------------|----------------|----------------|--------------------|

|                  |      |     |      |      |      |
|------------------|------|-----|------|------|------|
| <b>L4-40wt</b>   | 11.0 | 9.7 | 0.6  | 1.29 | 12.6 |
| <b>L4Fh-40wt</b> | 9.0  | 8.2 | 1.98 | 1.26 | 12.6 |

The theoretical maximum inter-lamellar  $d$ -spacing for an  $L_\beta$  phase can be estimated as[40]

$$d_{max} = \frac{10^{24}\sqrt{3}}{d_{WAXS}^2 C_a N_a} \quad (5)$$

where  $C_a$  is the total surfactant concentration in mol/l,  $N_a$  is the Avogadro number, and  $d_{WAXS}$  is the lattice constant obtained from the WAXS peak. The resulting  $d_{max}$  is 12.6 nm. Considering that  $I_{L\beta 1}$  and  $I_{L\beta 2}$  are proportional to the relative amount of the two lamellar phases, the  $L_\beta$  phase-swell was approximately 73% for the L4-40wt sample and 69% for the L4Fh-40wt sample. It is reasonable to assume that the Fh nanoparticles are located between the lamellar layers. Moreover, it has been demonstrated that nanoparticles can influence  $d$ -spacing in the lamellar phase, inducing bilayer attraction by suppressing layer undulations.[41–46] The power law of 2.2 at low- $q$  for the L4Fh-40wt sample is a strong indication of this phenomenon.

### 3.2 Entrapping Fh nanoparticles in the shear-induced MLVs

The 40 wt.% L4 and L4Fh lamellar phases were subjected to shear flow using a Taylor-Couette geometry (gap = 0.704 mm) to induce the formation of multilamellar vesicles (MLVs) as reported for  $C_{12}E_4$  at 40wt.%.[21,22] The steady-state viscosities obtained by transient experiments (Figure 2C and 2D) are shown in Figure 2A as a function of the shear rate, ranging from  $10^{-1}$  to  $10^2$   $s^{-1}$  for both the L4-40wt and L4Fh-40wt systems. The flow curve reveals three distinct regimes: the first regime represents slight shear thinning due to alignment of the lamellae in the flow direction[47], the second regime represents shear thickening due to MLV formation[15,17], and the third regime represents shear thinning due to the deformation of the densely packed MLV.[48] The maximum in the shear thickening region is shifted to a higher shear rate for L4Fh-40wt as can be seen also

1  
 2  
 3  
 4 from the transient experiments (Figure 2D), indicating higher bending rigidity with a more  
 5 pronounced viscosity maximum than that observed for the L4-40wt system. The onset of the L $\alpha$ -  
 6 to-MLV transition for the L4-40wt and the L4Fh-40wt is then 0.5 s<sup>-1</sup> and 5 s<sup>-1</sup>, respectively. The  
 7 corresponding shear rate-shear stress data (Figure 2B) reveal unusual behaviour for the L4Fh-40wt  
 8 system that can be interpreted in terms of the Johnson–Segalman (JS) model similarly to Olmsted  
 9 *et al.*[49,50] approach for rod particles, in which a possible phase separation *via* spinodal  
 10 decomposition can lead to shear banding.[51–55] This phenomenon requires further investigation.  
 11 Instead, the aqueous Fh nanoparticle dispersion shows Newtonian behavior (supplementary  
 12 material).  
 13  
 14  
 15  
 16  
 17  
 18  
 19  
 20  
 21  
 22  
 23  
 24  
 25  
 26  
 27  
 28  
 29  
 30  
 31  
 32  
 33  
 34  
 35  
 36  
 37  
 38  
 39  
 40  
 41  
 42  
 43  
 44  
 45  
 46  
 47  
 48  
 49  
 50  
 51  
 52  
 53  
 54  
 55  
 56  
 57  
 58  
 59  
 60  
 61  
 62  
 63  
 64  
 65

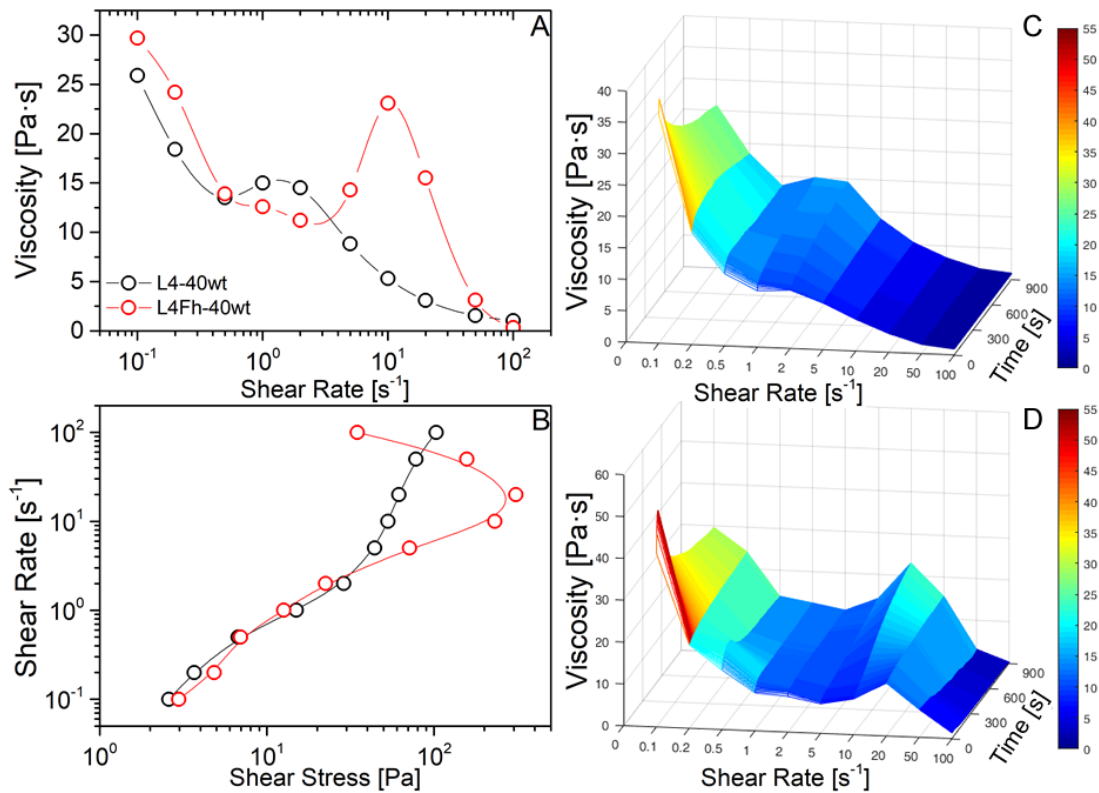
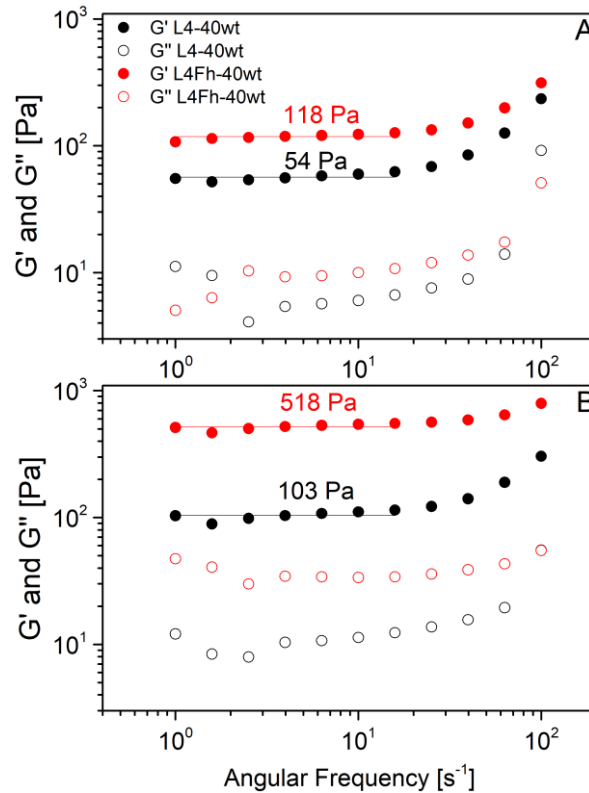


**Figure 2.** Steady-state viscosity as a function of the shear rate (A) and corresponding shear rate-shear stress plot (B) for the 40 wt.% L4 lamellar phase (L4-40wt) and the 40 wt.% L4 lamellar phase prepared in the Fh dispersion (L4Fh-40wt). Three-dimensional plots of the transient experiments performed to obtain the steady-state values are reported for both the L4-40wt (C) and

L4Fh-40wt systems (D). The color scale indicates viscosity values from 0 (blue) to 55 (red) Pa s to facilitate comparisons between the two systems.

The frequency sweep of the planar lamellar phase before applying shear flow and the corresponding frequency sweep after applying a shear rate of  $5 \text{ s}^{-1}$  are shown in Figure 3A and 3B, respectively, for the L4-40wt and L4Fh-40wt systems. The oscillatory measurement before the transient viscosity experiment (i.e. before applying shear flow) shows a storage modulus  $G'$  higher than the loss modulus  $G''$  over the frequency range of 1 to 100 rad/s. After the transient viscosity experiment at a shear rate of  $5 \text{ s}^{-1}$ ,  $G''$  increased only for the L4Fh-40wt system while  $G'$  increased for both systems, 2-fold for the L4-40wt and 5-fold for the L4Fh-40wt systems. The larger gap between  $G'$  and  $G''$  and the corresponding shear thickening indicate the MLV formation.[56]



1  
2  
3  
4 **Figure 3.** Frequency sweep measurements before (A) and after (B) applying a shear rate of  $5 \text{ s}^{-1}$   
5  
6 to the 40 wt.% L4 lamellar phase (L4-40wt) and for the 40 wt.% L4 lamellar phase prepared in the  
7  
8 Fh dispersion (L4Fh-40wt). The red and black lines are linear fitting of the data.  
9

10  
11  
12 The key contribution to the elastic modulus  $G'$  may arise from restricted motion due to vesicle-  
13  
14 vesicle interaction along with the length scale corresponding to the MLV size or the  $d$ -spacing. To  
15  
16 determine the effect of the  $d$ -spacing on the bilayer bending rigidity,  $K$ , we applied the approach  
17  
18 of Colafemmina *et al.*[31],  
19

$$K = \frac{4}{n} \frac{G'}{\tan^2 \theta} \bar{d}^3 \quad (6)$$

20  
21  
22 where here,  $\bar{d}$  is the weighted average of the  $d$ -spacing with respect to the  $I_{L\beta 1}$  and  $I_{L\beta 2}$  scattering  
23  
24 intensities,  $2\theta$  is the top angle of the cone over which two neighboring MLVs interact ( $\tan^2 \theta =$   
25  
26  $0.2$ ),  $n$  is the number of neighbours ( $\sim 10$ ), and  $G'$  is the value obtained at low angular frequency  
27  
28 from Figure 3. The bending rigidity of the L4-40wt in the MLV state is then  $\sim 0.05 \text{ k}_b\text{T}$ , while the  
29  
30 bending rigidity of the L4Fh-40wt is  $\sim 0.17 \text{ k}_b\text{T}$  in the MLV state. However, the bending rigidity  
31  
32 of the C<sub>12</sub>E<sub>4</sub> planar lamellar phase is known to be  $\sim 4.2 \text{ k}_b\text{T}$ . [57] The larger bending modulus of the  
33  
34 planar lamellae than the MLV states is due to the loss of out-of-plane membrane fluctuations  
35  
36 induced by the shear flow that opposes the Helfrich entropic repulsion, suggesting a loss of  
37  
38 resistance to compression in the MLV states. [58] The mechanical tension of the membrane is then  
39  
40 affected by the mean and spontaneous curvatures of the vesicle and by its shape. [59]  
41  
42  
43  
44  
45  
46  
47  
48  
49

#### 50 51 52 **4. Conclusions**

53  
54 We demonstrate here that Fh nanoparticles can be entrapped in a Brij L4 metastable lamellar  
55  
56 phase at 40 wt.%, generating a kinetically stable system.  
57  
58  
59  
60  
61  
62  
63  
64  
65

1  
2  
3  
4 The Fh nanoparticles affect the  $d$ -spacing of the lamellar phase, inducing bilayer attraction by  
5 suppressing layer undulations. This evidence is in agreement with a previous study of C<sub>12</sub>E<sub>4</sub> and  
6 silica nanoparticles, demonstrating the presence of nanoparticles in the bilayer spacing.[45] These  
7 results are also consistent with simulations of nanoparticles entrapped in the lamellar phase of  
8 diblock copolymers,[60] which have proven that spherical nanoparticles increases the strength of  
9 the interaction between the nanoparticles and blocks. Moreover, increasing the nanoparticle radius  
10 and/or volume fraction affects the degree of order of the lamellar phase until a bicontinuous  
11 morphology is formed.[60] Other simulations on zwitterionic unilamellar vesicles have shown that  
12 nanoparticles with a low-density charge occupy the centre of the vesicle membrane.[61] However,  
13 when the surface charge density of the nanoparticles increases, the positively charged  
14 nanoparticles are repulsed by the vesicles.[61]

15  
16 Here we highlighted for the first time that multilamellar vesicle formation under shear flow is  
17 affected by the presence of the nanoparticles in that a higher shear rate is needed to form the MLV  
18 state than for a lamellar phase free of nanoparticles. The bilayer bending rigidity of the lamellar  
19 phase in the MLV state is strongly affected by the presence of Fh nanoparticles. We have  
20 demonstrated that highly positively charged nanoparticles, but slightly larger than the  $d$ -spacing  
21 can be entrapped in a nonionic lamellar phase, indicating that their charge is compensated by the  
22 absorption of the alkyl carbon chain of the surfactant molecules in the bilayer thickness, an  
23 important insight in understanding the relationship between nanoparticle size and nanoparticle-  
24 bilayers interactions.

25  
26 Based on these results, we envision that ferrihydrite nanoparticles could be delivered in a  
27 controlled way using the kinetic stability of the MLV state for a variety of purposes such as  
28  
29  
30  
31  
32  
33  
34  
35  
36  
37  
38  
39  
40  
41  
42  
43  
44  
45  
46  
47  
48  
49  
50  
51  
52  
53  
54  
55  
56  
57  
58  
59  
60  
61  
62  
63  
64  
65

1  
2  
3  
4 trapping toxic materials. Moreover, further studies on the probable shear banding phenomena and  
5  
6 on the interplay with the non-ionic surfactants are of key interest.  
7  
8  
9

## 10 11 ACKNOWLEDGMENT

12  
13  
14 I am grateful to Prof. Ulf Olsson (Lund University, Sweden) for discussions on small-angle  
15 scattering techniques and lyotropic liquid crystals and to Prof. Per Persson (Lund University,  
16 Sweden) for an introduction to iron-based nanoparticles. I thank “Fondazione Puglia” (Bari, Italy)  
17 for supporting the purchase of rheometer as well as Dr. Riccardo Di Ciuccio and Dr. Matera Sergio  
18 (Anton Paar, Torino, Italy) for the stimulating rheological discussions.  
19  
20  
21  
22  
23  
24  
25  
26  
27  
28  
29  
30  
31  
32

## 33 REFERENCES

- 34  
35 [1] R.M. Cornell, U. Schwertmann, Transformations, in: The Iron Oxides, Wiley-VCH Verlag  
36 GmbH & Co. KGaA, Weinheim, FRG, 2003: pp. 365–407.  
37  
38 <https://doi.org/10.1002/3527602097.ch14>.  
39  
40  
41  
42  
43 [2] T. Hiemstra, Formation, stability, and solubility of metal oxide nanoparticles: Surface  
44 entropy, enthalpy, and free energy of ferrihydrite, *Geochimica et Cosmochimica Acta*. 158  
45 (2015) 179–198. <https://doi.org/10.1016/j.gca.2015.02.032>.  
46  
47  
48  
49  
50  
51 [3] R.J.K.U. Ranatunga, C.T. Nguyen, B.A. Wilson, W. Shinoda, S.O. Nielsen, Molecular  
52 dynamics study of nanoparticles and non-ionic surfactant at an oil–water interface, *Soft*  
53 *Matter*. 7 (2011) 6942–6952. <https://doi.org/10.1039/C1SM05145H>.  
54  
55  
56  
57  
58  
59  
60  
61  
62  
63  
64  
65

- 1  
2  
3  
4 [4] J.F.W. Bowles, Hydroxides, Encyclopedia of Geology. (2021) 442–451.  
5  
6 <https://doi.org/10.1016/B978-0-08-102908-4.00162-4>.  
7  
8  
9  
10 [5] F.M. Michel, L. Ehm, S.M. Antao, P.L. Lee, P.J. Chupas, G. Liu, D.R. Strongin, M.A.A.  
11  
12 Schoonen, B.L. Phillips, J.B. Parise, The Structure of Ferrihydrite, a Nanocrystalline  
13  
14 Material, Science. 316 (2007) 1726–1729. <https://doi.org/10.1126/science.1142525>.  
15  
16  
17  
18 [6] T. Hiemstra, Surface and mineral structure of ferrihydrite, Geochimica et Cosmochimica  
19  
20 Acta. 105 (2013) 316–325. <https://doi.org/10.1016/J.GCA.2012.12.002>.  
21  
22  
23  
24 [7] L. Gentile, T. Wang, A. Tunlid, U. Olsson, P. Persson, Ferrihydrite Nanoparticle  
25  
26 Aggregation Induced by Dissolved Organic Matter, The Journal of Physical Chemistry A.  
27  
28 122 (2018) 7730–7738. <https://doi.org/10.1021/acs.jpca.8b05622>.  
29  
30  
31  
32 [8] V.M. Yuwono, N.D. Burrows, J.A. Soltis, T. Anh Do, R. Lee Penn, Aggregation of  
33  
34 ferrihydrite nanoparticles in aqueous systems, Faraday Discussions. 159 (2012) 235.  
35  
36 <https://doi.org/10.1039/c2fd20115a>.  
37  
38  
39  
40 [9] D.B. Hausner, N. Bhandari, A.M. Pierre-Louis, J.D. Kubicki, D.R. Strongin, Ferrihydrite  
41  
42 reactivity toward carbon dioxide, Journal of Colloid and Interface Science. 337 (2009) 492–  
43  
44 500. <https://doi.org/10.1016/j.jcis.2009.05.069>.  
45  
46  
47  
48 [10] U. Schwertmann, H. Fechter, The point of zero charge of natural and synthetic ferrihydrites  
49  
50 and its relation to adsorbed silicate, Clay Minerals. 17 (1982) 471–476.  
51  
52 <https://doi.org/10.1180/CLAYMIN.1982.017.4.10>.  
53  
54  
55  
56 [11] C. Tian, J. Feng, H.J. Cho, S.S. Datta, R.K. Prud'homme, Adsorption and Denaturation of  
57  
58  
59  
60  
61  
62  
63  
64  
65

1  
2  
3  
4 Structured Polymeric Nanoparticles at an Interface, *Nano Letters*. 18 (2018) 4854–4860.  
5  
6 <https://doi.org/10.1021/ACS.NANOLETT.8B01434>.  
7  
8  
9

10 [12] V. Sorichetti, V. Hugouvieux, W. Kob, Structure and Dynamics of a Polymer–Nanoparticle  
11 Composite: Effect of Nanoparticle Size and Volume Fraction, *Macromolecules*. 51 (2018)  
12 5375–5391. <https://doi.org/10.1021/ACS.MACROMOL.8B00840>.  
13  
14

15  
16  
17  
18 [13] D.J. Mitchell, G.J.T. Tiddy, L. Waring, T. Bostock, M.P. McDonald, Phase behaviour of  
19 polyoxyethylene surfactants with water. Mesophase structures and partial miscibility (cloud  
20 points), *Journal of the Chemical Society, Faraday Transactions 1: Physical Chemistry in*  
21 *Condensed Phases*. 79 (1983) 975–1000. <https://doi.org/10.1039/F19837900975>.  
22  
23  
24  
25

26  
27  
28  
29 [14] C. Leal, A. Bilalov, B. Lindman, The effect of postadded ethylene glycol surfactants on  
30 DNA-cationic surfactant/water mesophases, *Journal of Physical Chemistry B*. 113 (2009)  
31 9909–9914. <https://doi.org/10.1021/jp810185k>.  
32  
33  
34  
35

36  
37  
38 [15] D. Roux, F. Nallet, O. Diat, Rheology of lyotropic lamellar phases, *EPL*. 24 (1993) 53–58.  
39  
40 <https://doi.org/10.1209/0295-5075/24/1/009>.  
41  
42

43 [16] O. Diat, D. Roux, F. Nallet, Effect of shear on a lyotropic lamellar phase, *Journal de*  
44 *Physique II*. 3 (1993) 1427–1452. <https://doi.org/10.1051/JP2:1993211>.  
45  
46  
47

48  
49 [17] L. Gentile, M.A. Behrens, S. Balog, K. Mortensen, G.A. Ranieri, U. Olsson, Dynamic phase  
50 diagram of a nonionic surfactant lamellar phase, *Journal of Physical Chemistry B*. 118  
51 (2014) 3622–3629. <https://doi.org/10.1021/jp5009797>.  
52  
53  
54  
55

56  
57  
58 [18] L. Gentile, L. Coppola, S. Balog, K. Mortensen, G.A. Ranieri, U. Olsson, Phase Coexistence  
59  
60  
61  
62  
63  
64  
65

1  
2  
3  
4 in a Dynamic Phase Diagram, ChemPhysChem. 16 (2015).  
5  
6 <https://doi.org/10.1002/cphc.201500237>.  
7  
8

9  
10 [19] L. Gentile, K. Mortensen, C.O. Rossi, U. Olsson, G.A. Ranieri, Multi-lamellar vesicle  
11 formation in a long-chain nonionic surfactant: C<sub>16</sub>E<sub>4</sub>/D  
12 <sub>2</sub>O system, Journal of Colloid and Interface Science. 362 (2011).  
13  
14 <https://doi.org/10.1016/j.jcis.2011.06.053>.  
15  
16  
17

18  
19 [20] F. Nettesheim, J. Zipfel, U. Olsson, F. Renth, P. Lindner, W. Richtering, Pathway of the  
20 shear-induced transition between planar lamellae and multilamellar vesicles as studied by  
21 time-resolved scattering techniques, Langmuir. 19 (2003) 3603–3618.  
22  
23 <https://doi.org/10.1021/LA026654Y>.  
24  
25  
26  
27

28  
29 [21] T.D. Le, U. Olsson, K. Mortensen, Packing states of multilamellar vesicles in a nonionic  
30 surfactant system, Physical Chemistry Chemical Physics. 3 (2001) 1310–1316.  
31  
32 <https://doi.org/10.1039/B006747O>.  
33  
34  
35  
36  
37

38  
39 [22] Y. Suganuma, M. Imai, T. Kato, U. Olsson, T. Takahashi, Order–Disorder Transition of  
40 Nonionic Onions under Shear Flow, Langmuir. 26 (2010) 7988–7995.  
41  
42 <https://doi.org/10.1021/LA904862E>.  
43  
44  
45  
46  
47

48  
49 [23] J. Teixeira, Small-angle scattering by fractal systems, Journal of Applied Crystallography.  
50 21 (1988) 781–785. <https://doi.org/10.1107/S0021889888000263>.  
51  
52  
53

54  
55 [24] S. Prevost, T. Lopian, M. Pleines, O. Diat, T. Zemb, Small-angle scattering and  
56 morphologies of ultra-flexible microemulsions 1, J. Appl. Cryst. 49 (2016) 2063–2072.  
57  
58 <https://doi.org/10.1107/S1600576716016150>.  
59  
60  
61  
62  
63  
64  
65

- 1  
2  
3  
4 [25] H. Guénet, M. Davranche, D. Vantelon, J. Gigault, S. Prévost, O. Taché, S. Jaksch, M.  
5  
6 Pédrot, V. Dorcet, A. Boutier, J. Jestin, Characterization of iron–organic matter nano-  
7  
8 aggregate networks through a combination of SAXS/SANS and XAS analyses: impact on  
9  
10 As binding, *Environ. Sci.: Nano.* 4 (2017) 938–954. <https://doi.org/10.1039/C6EN00589F>.  
11  
12  
13  
14  
15 [26] P.J. Murphy, A.M. Posner, J.P. Quirk, Characterization of hydrolyzed ferric ion solutions a  
16  
17 comparison of the effects of various anions on the solutions, *Journal of Colloid and Interface*  
18  
19 *Science.* 56 (1976) 312–319. [https://doi.org/10.1016/0021-9797\(76\)90256-3](https://doi.org/10.1016/0021-9797(76)90256-3).  
20  
21  
22  
23 [27] D.E. Janney, J.M. Cowley, P.R. Buseck, Transmission Electron Microscopy of Synthetic 2-  
24  
25 and 6-Line Ferrihydrite, *Clays and Clay Minerals* 2000 48:1. 48 (2000) 111–119.  
26  
27 <https://doi.org/10.1346/CCMN.2000.0480114>.  
28  
29  
30  
31  
32 [28] T. Hiemstra, W.H. Van Riemsdijk, A surface structural model for ferrihydrite I: Sites related  
33  
34 to primary charge, molar mass, and mass density, *Geochimica et Cosmochimica Acta.* 73  
35  
36 (2009) 4423–4436. <https://doi.org/10.1016/j.gca.2009.04.032>.  
37  
38  
39  
40 [29] J.M. Seddon, R.H. Templer, Polymorphism of lipid-water systems, *Handbook of Biological*  
41  
42 *Physics.* 1 (1995) 97–160. [https://doi.org/10.1016/S1383-8121\(06\)80020-5](https://doi.org/10.1016/S1383-8121(06)80020-5).  
43  
44  
45  
46 [30] G.M. Eccleston, Functions of mixed emulsifiers and emulsifying waxes in dermatological  
47  
48 lotions and creams, *Colloids and Surfaces A: Physicochemical and Engineering Aspects.*  
49  
50 123–124 (1997) 169–182. [https://doi.org/10.1016/S0927-7757\(96\)03846-0](https://doi.org/10.1016/S0927-7757(96)03846-0).  
51  
52  
53  
54 [31] G. Colafemmina, G. Palazzo, H. Mateos, S. Amin, A.L. Fameau, U. Olsson, L. Gentile, The  
55  
56 cooling process effect on the bilayer phase state of the CTAC/cetearyl alcohol/water  
57  
58 surfactant gel, *Colloids and Surfaces A: Physicochemical and Engineering Aspects.* 597  
59  
60  
61  
62  
63  
64  
65

1  
2  
3  
4 (2020) 124821. <https://doi.org/10.1016/J.COLSURFA.2020.124821>.  
5  
6

7  
8 [32] S. Nappini, M. Bonini, F. Ridi, P. Baglioni, Structure and permeability of  
9 magnetoliposomes loaded with hydrophobic magnetic nanoparticles in the presence of a  
10 low frequency magnetic field, *Soft Matter*. 7 (2011) 4801–4811.  
11  
12 <https://doi.org/10.1039/C0SM01264E>.  
13  
14

15  
16  
17  
18 [33] D. Roux, C.R. Safinya, A synchrotron X-ray study of competing undulation and  
19 electrostatic interlayer interactions in fluid multimembrane lyotropic phases, *Journal de*  
20 *Physique*. 49 (1988) 307–318. <https://doi.org/10.1051/JPHYS:01988004902030700>.  
21  
22

23  
24 [34] N. Lei, C.R. Safinya, R.F. Bruinsma, Discrete Harmonic Model for Stacked Membranes:  
25 Theory and Experiment, *Journal de Physique II*. 5 (1995) 1155–1163.  
26  
27 <https://doi.org/10.1051/JP2:1995174>.  
28  
29

30  
31 [35] M. Mihailescu, M. Monkenbusch, J. Allgaier, H. Frielinghaus, D. Richter, B. Jakobs, T.  
32 Sottmann, Neutron scattering study on the structure and dynamics of oriented lamellar phase  
33 microemulsions, *Physical Review E*. 66 (2002) 041504.  
34  
35 <https://doi.org/10.1103/PhysRevE.66.041504>.  
36  
37

38  
39 [36] L. Wang, X. Xin, M. Yang, X. Ma, Z. Feng, R. Chen, J. Shen, S. Yuan, Comparative study  
40 of n-dodecyl tetraethylene monoether lyotropic liquid crystals incorporated with graphene  
41 and graphene oxide, *Physical Chemistry Chemical Physics*. 16 (2014) 20932–20940.  
42  
43 <https://doi.org/10.1039/C4CP02634A>.  
44  
45

46  
47 [37] X. Xin, H. Li, E. Kalwarczyk, A. Kelm, M. Fiałkowski, E. Gorecka, D. Pocięcha, R. Hołyst,  
48  
49 Single-Walled Carbon Nanotube/Lyotropic Liquid Crystal Hybrid Materials Fabricated by  
50  
51  
52  
53  
54  
55  
56

- 1  
2  
3  
4 a Phase Separation Method in the Presence of Polyelectrolyte, *Langmuir*. 26 (2010) 8821–  
5  
6  
7 8828. <https://doi.org/10.1021/LA101032D>.  
8  
9
- [38] F. Castro-Roman, L. Porcar, G. Porte, C. Ligoure, Quantitative analysis of lyotropic  
10  
11 lamellar phases SANS patterns in powder oriented samples, *The European Physical Journal*  
12  
13 *E*. 18 (2005) 259–272. <https://doi.org/10.1140/EPJE/E2005-00029-6>.  
14  
15  
16  
17
- [39] F. Nallet, R. Laversanne, D. Roux, Modelling X-ray or neutron scattering spectra of  
18  
19 lyotropic lamellar phases: interplay between form and structure factors, *Journal de*  
20  
21 *Physique II*. 3 (1993) 487–502. <https://doi.org/10.1051/jp2:1993146>.  
22  
23  
24  
25
- [40] T. Iwata, Lamellar gel network, in: *Cosmetic Science and Technology: Theoretical*  
26  
27 *Principles and Applications*, Elsevier Inc., 2017: pp. 415–447.  
28  
29  
30  
31  
32 <https://doi.org/10.1016/B978-0-12-802005-0.00025-2>.  
33  
34
- [41] L. Cipelletti, L. Ramos, Slow dynamics in glassy soft matter, *Journal of Physics Condensed*  
35  
36 *Matter*. 17 (2005). <https://doi.org/10.1088/0953-8984/17/6/r01>.  
37  
38  
39  
40
- [42] M. Imai, Y. Suganuma, K. Nakaya, S. Komura, Surfactant mesophases mediated by  
41  
42 colloidal particles, *J. Phys.: Condens. Matter*. 17 (2005) 2929–2935.  
43  
44  
45  
46  
47 <https://doi.org/10.1088/0953-8984/17/31/020>.  
48
- [43] Y. Suganuma, M. Imai, K. Nakaya, Repulsive interlamellar interaction induced by addition  
49  
50 of colloidal particles, *Urn:Issn:0021-8898*. 40 (2007) s303–s306.  
51  
52  
53  
54  
55  
56  
57 <https://doi.org/10.1107/S0021889807010345>.
- [44] G. Salamat, E.W. Kaler, Colloidal dispersions in lyotropic lamellar phases, *Langmuir*. 15

- 1  
2  
3  
4 (1999) 5414–5421. <https://doi.org/10.1021/la980928t>.
- 5  
6  
7  
8 [45] E. Venugopal, V.K. Aswal, G. Kumaraswamy, Nanoparticle Size Controls Aggregation in  
9 Lamellar Nonionic Surfactant Mesophase, *Langmuir*. 29 (2013) 9643–9650.  
10 <https://doi.org/10.1021/LA4021977>.  
11  
12  
13  
14  
15  
16 [46] M. Mendoza, L. Caselli, A. Salvatore, C. Montis, D. Berti, Nanoparticles and organized  
17 lipid assemblies: From interaction to design of hybrid soft devices, *Soft Matter*. 15 (2019)  
18 8951–8970. <https://doi.org/10.1039/c9sm01601e>.  
19  
20  
21  
22  
23  
24 [47] C.R. Safinya, E.B. Sirota, R.F. Bruinsma, C. Jeppesen, R.J. Plano, L.J. Wenzel, Structure  
25 of membrane surfactant and liquid crystalline smectic lamellar phases under flow, *Science*.  
26 261 (1993) 588–591. <https://doi.org/10.1126/science.261.5121.588>.  
27  
28  
29  
30  
31  
32  
33 [48] S. Fujii, W. Richtering, Size and viscoelasticity of spatially confined multilamellar vesicles,  
34 *The European Physical Journal E* 2006 19:2. 19 (2006) 139–148.  
35 <https://doi.org/10.1140/EPJE/E2006-00015-6>.  
36  
37  
38  
39  
40  
41 [49] P.D. Olmsted, C.Y.D. Lu, Phase separation of rigid-rod suspensions in shear flow, *Physical*  
42 *Review E - Statistical Physics, Plasmas, Fluids, and Related Interdisciplinary Topics*. 60  
43 (1999) 4397–4415. <https://doi.org/10.1103/PhysRevE.60.4397>.  
44  
45  
46  
47  
48  
49 [50] P.D. Olmsted, Perspectives on shear banding in complex fluids, *Rheologica Acta* 2008 47:3.  
50 47 (2008) 283–300. <https://doi.org/10.1007/S00397-008-0260-9>.  
51  
52  
53  
54  
55 [51] S.M. Fielding, Linear Instability of Planar Shear Banded Flow, *Physical Review Letters*. 95  
56 (2005) 134501. <https://doi.org/10.1103/PhysRevLett.95.134501>.  
57  
58  
59  
60  
61  
62  
63  
64  
65

- 1  
2  
3  
4 [52] L. Gentile, B.F.B. Silva, S. Lages, K. Mortensen, J. Kohlbrecher, U. Olsson, Rheochaos and  
5  
6 flow instability phenomena in a nonionic lamellar phase, *Soft Matter*. 9 (2013).  
7  
8 <https://doi.org/10.1039/c2sm27101j>.  
9  
10  
11  
12 [53] R. Besseling, L. Isa, P. Ballesta, G. Petekidis, M.E. Cates, W.C.K. Poon, Shear Banding  
13  
14 and Flow-Concentration Coupling in Colloidal Glasses, *Physical Review Letters*. 105  
15  
16 (2010) 268301. <https://doi.org/10.1103/PhysRevLett.105.268301>.  
17  
18  
19  
20  
21 [54] M.A. Calabrese, S.A. Rogers, L. Porcar, N.J. Wagner, Understanding steady and dynamic  
22  
23 shear banding in a model wormlike micellar solution, *Journal of Rheology*. 60 (2016) 1001.  
24  
25 <https://doi.org/10.1122/1.4961035>.  
26  
27  
28  
29 [55] L. Zhou, R.H. Ewoldt, L.P. Cook, G.H. McKinley, Probing Shear- Banding Transitions of  
30  
31 Entangled Liquids Using Large Amplitude Oscillatory Shearing (LAOS) Deformations,  
32  
33 *AIP Conference Proceedings*. 1027 (2008) 189. <https://doi.org/10.1063/1.2964629>.  
34  
35  
36  
37  
38 [56] L. Gentile, B.F.B. Silva, S. Balog, K. Mortensen, U. Olsson, Structural transitions induced  
39  
40 by shear flow and temperature variation in a nonionic surfactant/water system, *Journal of*  
41  
42 *Colloid and Interface Science*. 372 (2012) 32–39.  
43  
44 <https://doi.org/10.1016/j.jcis.2012.01.027>.  
45  
46  
47  
48 [57] L. Gentile, B.F.B. Silva, S. Balog, K. Mortensen, U. Olsson, Structural transitions induced  
49  
50 by shear flow and temperature variation in a nonionic surfactant/water system, *Journal of*  
51  
52 *Colloid and Interface Science*. 372 (2012) 32–39.  
53  
54 <https://doi.org/10.1016/j.jcis.2012.01.027>.  
55  
56  
57  
58  
59 [58] L. Porcar, G.G. Warr, W.A. Hamilton, P.D. Butler, Shear-induced collapse in a lyotropic  
60  
61  
62  
63  
64  
65

1  
2  
3  
4 lamellar phase, Physical Review Letters. 95 (2005).  
5  
6  
7 <https://doi.org/10.1103/PhysRevLett.95.078302>.  
8  
9

10 [59] R. Lipowsky, Coupling of bending and stretching deformations in vesicle membranes,  
11 Advances in Colloid and Interface Science. 208 (2014) 14–24.  
12  
13 <https://doi.org/10.1016/J.CIS.2014.02.008>.  
14  
15  
16  
17

18 [60] L. He, L. Zhang, H. Liang, The effects of nanoparticles on the lamellar phase separation of  
19 diblock copolymers, Journal of Physical Chemistry B. 112 (2008) 4194–4203.  
20  
21 <https://doi.org/10.1021/jp0757412>.  
22  
23  
24  
25

26 [61] Linying Liu, Jianhua Zhang, Xiaowei Zhao, Zheng Mao, Na Liu, Youyu Zhang, Q.  
27 Huo Liu, Interaction between charged nanoparticles and vesicles: coarse-grained molecular  
28 dynamics simulations, Physical Chemistry Chemical Physics. 18 (2016) 31946–31957.  
29  
30 <https://doi.org/10.1039/C6CP05998H>.  
31  
32  
33  
34  
35  
36  
37  
38  
39  
40  
41  
42  
43  
44  
45  
46  
47  
48  
49  
50  
51  
52  
53  
54  
55  
56  
57  
58  
59  
60  
61  
62  
63  
64  
65

1  
2  
3  
4 **Figure Captions**  
5  
6  
7

8  
9 **Figure 1.** Radially averaged small- and wide-angle X-ray scattering (SAXS and WAXS) profiles  
10  
11 (A) at 25 °C of 60 wt.% in water of the ferrihydrite nanoparticle dispersion (Fh-60wt; red dot), i.e.  
12  
13 0.96 g/l, 40 wt.% L4 nonionic surfactant in H<sub>2</sub>O (L4-40wt; blue dot), and 40 wt. % L4 nonionic  
14  
15 surfactant in Fh nanoparticle dispersion (L4Fh-40wt; black dot). The green line shows the best fit  
16  
17 for a fractal structure with a primary building block of polydisperse spheres, based on the Teixeira  
18  
19 model,[23] eq. 1-3. The bottom-left inset shows a semi-log plot of the scattering profiles along  
20  
21 with the best fit for the lamellar phase following Prevost *et al.*,[24] eq. 4, for the L4-40wt (pink)  
22  
23 and L4Fh-40wt (orange) samples. The top-right inset shows a linear-linear plot of the WAXS  
24  
25 profiles, with a peak at  $q = 1.38 \text{ \AA}^{-1}$  for both the L4-40wt and L4Fh-40wt samples. 2D SAXS  
26  
27 pattern in the low  $q$ -range for L4-40wt (B), L4Fh-40wt (C) and Fh-60wt (D).  
28  
29  
30  
31  
32

33  
34 **Figure 2.** Steady-state viscosity as a function of the shear rate (A) and corresponding shear rate-  
35  
36 shear stress plot (B) for the 40 wt.% L4 lamellar phase (L4-40wt) and the 40 wt.% L4 lamellar  
37  
38 phase prepared in the Fh dispersion (L4Fh-40wt). Three-dimensional plots of the transient  
39  
40 experiments performed to obtain the steady-state values are reported for both the L4-40wt (C) and  
41  
42 L4Fh-40wt systems (D). The color scale indicates viscosity values from 0 (blue) to 55 (red) Pa s  
43  
44 to facilitate comparisons between the two systems.  
45  
46  
47  
48

49  
50 **Figure 3.** Frequency sweep measurements before (A) and after (B) applying a shear rate of  $5 \text{ s}^{-1}$   
51  
52 to the 40 wt.% L4 lamellar phase (L4-40wt) and for the 40 wt.% L4 lamellar phase prepared in the  
53  
54 Fh dispersion (L4Fh-40wt). The red and black lines are linear fitting of the data.  
55  
56  
57  
58  
59  
60  
61  
62  
63  
64  
65

## Tables

**Table 1.**  $d$ -spacing  $d_{L\beta 1} = 2\pi/q_{L\beta 1}^{peak}$  and  $d_{L\beta 2} = 2\pi/q_{L\beta 2}^{peak}$  for the 40 wt.% L4 lamellar phase in water (L4-40wt) and in the ferrihydrite dispersion (L4Fh-40wt), where  $q_{L\beta 1}^{peak}$  and  $q_{L\beta 2}^{peak}$  were obtained from SAXS profile fitting (eq. 4), and where  $I_{L\beta 1}$  and  $I_{L\beta 2}$  are the relative intensities. The theoretical maximum inter-lamellar  $d$ -spacing was calculated using eq. 5. All values are in nm.

|                  | $d_{L\beta 1}$ | $d_{L\beta 2}$ | $I_{L\beta 1}$ | $I_{L\beta 2}$ | $d_{L\beta}^{max}$ |
|------------------|----------------|----------------|----------------|----------------|--------------------|
| <b>L4-40wt</b>   | 11.0           | 9.7            | 0.6            | 1.29           | 12.6               |
| <b>L4Fh-40wt</b> | 9.0            | 8.2            | 1.98           | 1.26           | 12.6               |

1  
2  
3  
4  
5  
6  
7  
8  
9  
10  
11  
12  
13  
14  
15  
16  
17  
18  
19  
20  
21  
22  
23  
24  
25  
26  
27  
28  
29  
30  
31  
32  
33  
34  
35  
36  
37  
38  
39  
40  
41  
42  
43  
44  
45  
46  
47  
48  
49  
50  
51  
52  
53  
54  
55  
56  
57  
58  
59  
60  
61  
62  
63  
64  
65

## Supplementary material

# Ferrihydrite nanoparticles entrapped in shear-induced multilamellar vesicles

*Luigi Gentile*<sup>1,2\*</sup>

1. Department of Chemistry, University of Bari “Aldo Moro”, Via Orabona 4, Bari, 70126, Italy

2. Center of Colloid and Surface Science (CSGI) Bari Unit, Via Orabona 4, Bari, 70126, Italy

### AUTHOR INFORMATION

#### **Corresponding Author**

\*Luigi Gentile, Senior lecturer at the Department of Chemistry of the University of Bari “Aldo Moro”, 70125 Bari (Italy) [orcid.org/0000-0001-6854-2963](https://orcid.org/0000-0001-6854-2963) email: [luigi.gentile@uniba.it](mailto:luigi.gentile@uniba.it), Tel: +39 0805442033.

## 1. Normalization of the wide-angle X-ray scattering data

The 40 wt.% lamellar phase of a tetraethylene glycol monododecyl ether with  $M_n \sim 362$  (L4-40wt) and the 40 wt.% lamellar phase prepared in the ferrihydrite dispersion (L4Fh-40wt) show a peak in the WAXS regime centered at  $q_{WAXS} = 1.38 \text{ \AA}^{-1}$ , which implies a lateral packing of alkyl chain perpendicular to the bilayer indicating a gel lamellar phase  $L_{\beta}$ . [1–3] The peak is clearly coming from the lamellar phase as can be seen in Figure S1 where the H<sub>2</sub>O (background) is compared with the ferrihydrite dispersion diluted to 60 wt.% (Fh-60wt), L4-40wt and L4Fh-40wt as such is not due to a wrong background subtraction.

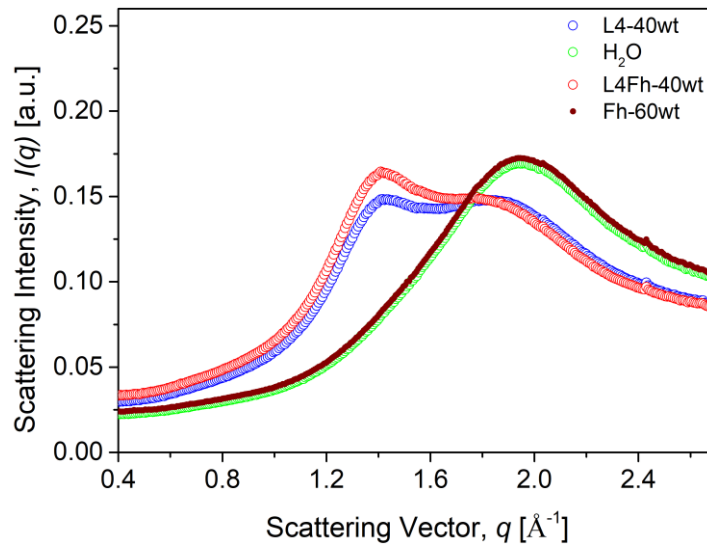


**Figure S1.** Wide-angle X-ray profiles in a linear-linear plot of the background (H<sub>2</sub>O), ferrihydrite dispersion diluted in H<sub>2</sub>O to 60 wt.% (Fh-60wt), 40 wt.% lamellar phase in H<sub>2</sub>O (L4-40wt) and 40 wt.% lamellar phase prepared using the ferrihydrite dispersion (L4Fh-40wt).

## 2. Dynamic light scattering and zeta-potential

The Zetasizer Nano ZS instrument from Malvern Instruments, Ltd., Worcestershire, UK, was used for a dynamic light scattering (DLS) measurement at  $\theta = 173^\circ$  in addition to an electrophoretic mobility measurement of the Ferrihydrite dispersion. The main volume-weighted distribution was

centered on the hydrodynamic radius,  $R_H$ , of 1.39 nm (Figure S2). The ratio between the radius of gyration,  $R_g$ , and  $R_H$ , for a solid sphere yields 0.775, i.e.  $R_g \sim 1$  nm close to 0.8 nm of the spherical primary building block,  $R_0$ , of the fractal aggregate in the SAXS analysis (main text). The goniometer system was equipped with a 4- mW He- Ne laser with an automatic laser attenuator, and the detection unit comprised an avalanche photodiode. The temperature was set to 25 °C. The Ferrihydrite dispersion was filled in disposable folded capillary cells, and the measurements were performed at a fixed scattering angle of 173° using a laser interferometric technique (laser Doppler electrophoresis), which enabled the determination of the electrophoretic mobility. In such an experiment, an electric field is applied to a dispersion of charged particles that move with a velocity ( $v = |\vec{v}|$ ), and the Doppler- shifted frequency of the incident laser beam caused by these moving particles is monitored. The velocity of a particle with radius  $R$  moving in an applied electric field,  $E = |\vec{E}|$ , is  $v = u_e E$ , where  $u_e$  is the electrophoretic mobility. The zeta potential,  $\zeta$ , was calculated from the Helmholtz- Smoluchowski equation.[4] The  $\zeta$  was +55 mV.

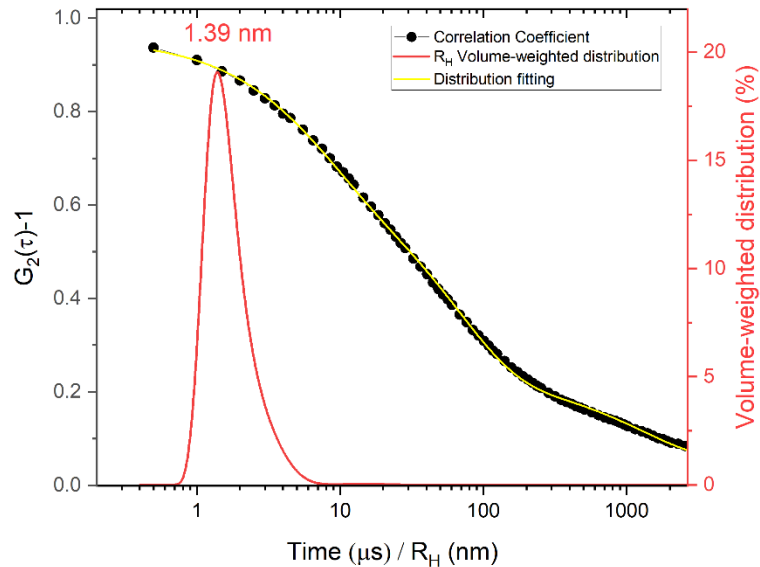


**Figure S2.** Correlation function and size distribution calculated by means of CONTIN algorithm for water Ferrihydrite nanoparticle dispersion.

### 3. Rheological behavior of Ferrihydrite dispersion

Figure S3 shows the Newtonian behaviour of the Ferrihydrite dispersion.

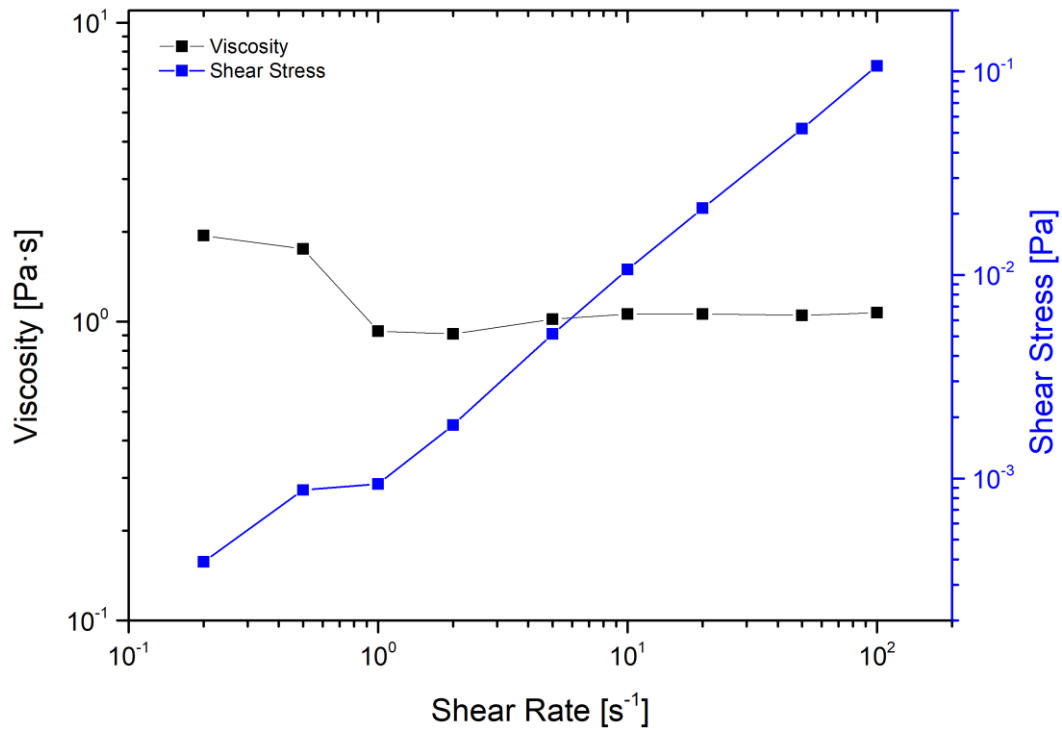


Figure S3. Steady-state viscosity and corresponding shear stress as a function of the shear rate for Ferrihydrite dispersion (Fh).

#### REFERENCES

- [1] J.M. Seddon, R.H. Templer, Polymorphism of lipid-water systems, Handbook of Biological Physics. 1 (1995) 97–160. [https://doi.org/10.1016/S1383-8121\(06\)80020-5](https://doi.org/10.1016/S1383-8121(06)80020-5).
- [2] G.M. Eccleston, Functions of mixed emulsifiers and emulsifying waxes in dermatological lotions and creams, Colloids and Surfaces A: Physicochemical and Engineering Aspects. 123–124 (1997) 169–182. [https://doi.org/10.1016/S0927-7757\(96\)03846-0](https://doi.org/10.1016/S0927-7757(96)03846-0).
- [3] G. Colafemmina, G. Palazzo, H. Mateos, S. Amin, A.L. Fameau, U. Olsson, L. Gentile, The cooling process effect on the bilayer phase state of the CTAC/cetaryl alcohol/water

1  
2  
3  
4  
5  
6  
7  
8  
9  
10  
11  
12  
13  
14  
15  
16  
17  
18  
19  
20  
21  
22  
23  
24  
25  
26  
27  
28  
29  
30  
31  
32  
33  
34  
35  
36  
37  
38  
39  
40  
41  
42  
43  
44  
45  
46  
47  
48  
49  
50  
51  
52  
53  
54  
55  
56  
57  
58  
59  
60  
61  
62  
63  
64  
65

surfactant gel, *Colloids and Surfaces A: Physicochemical and Engineering Aspects*. 597  
(2020) 124821. <https://doi.org/10.1016/J.COLSURFA.2020.124821>.

[4] F. Evans, H. Wennerström, *Colloidal domain : where physics, chemistry and biology meet*,  
Wiley-VCH, 1999.